

Hair cell synaptic dysfunction, auditory fatigue and thermal sensitivity in otoferlin Ile515Thr mutants

Nicola Strenzke^{1,2,*†}, Rituparna Chakrabarti^{2,3,4,†}, Hanan Al-Moyed^{4,5,†}, Alexandra Müller^{2,4,5}, Gerhard Hoch⁶, Tina Pangrsic^{2,7}, Gulnara Yamanbaeva^{1,2,4}, Christof Lenz^{8,9}, Kuan-Ting Pan⁸, Elisabeth Auge¹, Ruth Geiss-Friedlander¹⁰, Henning Urlaub^{2,8,9}, Nils Brose^{2,11}, Carolin Wichmann^{2,3,**} & Ellen Reisinger^{2,5,11,***}

Abstract

The multi-C₂ domain protein otoferlin is required for hearing and mutated in human deafness. Some *OTOF* mutations cause a mild elevation of auditory thresholds but strong impairment of speech perception. At elevated body temperature, hearing is lost. Mice homozygous for one of these mutations, *Otof*^{I515T/I515T}, exhibit a moderate hearing impairment involving enhanced adaptation to continuous or repetitive sound stimulation. In *Otof*^{I515T/I515T} inner hair cells (IHCs), otoferlin levels are diminished by 65%, and synaptic vesicles are enlarged. Exocytosis during prolonged stimulation is strongly reduced. This indicates that otoferlin is critical for the reformation of properly sized and fusion-competent synaptic vesicles. Moreover, we found sustained exocytosis and sound encoding to scale with the amount of otoferlin at the plasma membrane. We identified a 20 amino acid motif including an RXR motif, presumably present in human but not in mouse otoferlin, which reduces the plasma membrane abundance of Ile515Thr-otoferlin. Together, this likely explains the auditory synaptopathy at normal temperature and the temperature-sensitive deafness in humans carrying the Ile515Thr mutation.

Keywords auditory neuropathy; hair cell; hearing loss; otoferlin; ribbon synapse

Subject Categories Molecular Biology of Disease; Neuroscience

DOI 10.15252/embj.201694564 | Received 15 April 2016 | Revised 24 August 2016 | Accepted 13 September 2016 | Published online 11 October 2016

The EMBO Journal (2016) 35: 2519–2535

See also: **KB Avraham** (December 2016)

Introduction

Mutations in *OTOF*, the gene coding for the multi-C₂ domain protein otoferlin, cause human prelingual deafness DFNB9 (Yasunaga *et al*, 1999). Otoferlin is required for a late step in exocytosis in mouse inner hair cells (IHCs), as its absence nearly abolishes depolarization-induced exocytosis despite the presence of synaptic vesicles at the ribbon-type active zones (Roux *et al*, 2006). It was proposed that this phenotype reflects a role of otoferlin as a Ca²⁺ sensor of exocytosis (Roux *et al*, 2006; Johnson & Chapman, 2010), but this idea requires further experimental testing. Indeed, in the profoundly hearing impaired *pachanga* mouse model (*Otof*^{Pga/Pga}), which carries a point mutation in otoferlin (Schwander *et al*, 2007), only sustained exocytosis is impaired, while fast exocytosis, reporting the fusion of the readily releasable pool (RRP), is not (Pangrsic *et al*, 2010). The finding of impaired vesicle replenishment led to the hypothesis that otoferlin also functions in vesicle priming, which was subsequently supported by a recent study showing a reduction in short tethers connecting synaptic vesicles with the active zone membrane in otoferlin knockout (*Otof*^{−/−}) mice (Vogl *et al*, 2015). In addition to these putative roles in priming and fusion, otoferlin may be involved in exocytosis–endocytosis coupling via an

- 1 Auditory Systems Physiology Group, Department for Otolaryngology and InnerEarLab, University Medical Center Göttingen, Göttingen, Germany
 - 2 Collaborative Research Center 889 “Cellular Mechanisms of Sensory Processing”, Göttingen, Germany
 - 3 Molecular Architecture of Synapses Group, Institute for Auditory Neuroscience and InnerEarLab, University Medical Center Göttingen and Max Planck Institute of Experimental Medicine, Göttingen, Germany
 - 4 Göttingen Graduate School for Neurosciences, Biophysics, and Molecular Biosciences, Göttingen, Germany
 - 5 Molecular Biology of Cochlear Neurotransmission Group, Department for Otolaryngology and InnerEarLab, University Medical Center Göttingen, Göttingen, Germany
 - 6 Institute for Auditory Neuroscience and InnerEarLab, University Medical Center Göttingen and German Primate Center, Göttingen, Germany
 - 7 Synaptic Physiology of Mammalian Vestibular Hair Cells Group, Institute for Auditory Neuroscience and InnerEarLab, University Medical Center Göttingen and Max Planck Institute of Experimental Medicine, Göttingen, Germany
 - 8 Bioanalytical Mass Spectrometry Group, Max Planck Institute for Biophysical Chemistry, Göttingen, Germany
 - 9 Bioanalytics, Institute of Clinical Chemistry, University Medical Center Göttingen, Göttingen, Germany
 - 10 Department of Molecular Biology, University Medical Center Göttingen, Göttingen, Germany
 - 11 Department of Molecular Neurobiology, Max Planck Institute of Experimental Medicine, Göttingen, Germany
- *Corresponding author. Tel: +49 551 39 9688; E-mail: nstrenzke@med.uni-goettingen.de
 **Corresponding author. Tel: +49 551 39 61128; E-mail: carolin.wichmann@med.uni-goettingen.de
 ***Corresponding author. Tel: +49 551 39 9688; E-mail: ellen.reisinger@med.uni-goettingen.de
 †These authors contributed equally to this work

interaction with the clathrin adapter protein AP-2 (Duncker *et al*, 2013; Jung *et al*, 2015).

While most mutations in human *OTOF* lead to profound deafness, a defined set of missense mutations cause a striking non-syndromic recessive temperature-sensitive auditory synaptopathy (reviewed in Pangrsic *et al*, 2012) that is exceptional in several aspects. First, at normal body temperature, patients have near-normal pure tone hearing thresholds but impaired speech recognition, especially in background noise (Starr *et al*, 1998). Second, psychoacoustic testing of some patients revealed severe abnormalities of loudness adaptation to continuous pure tone stimulation, also called “auditory fatigue” (Wynne *et al*, 2013). Third, elevation of body temperature to $\geq 38.1^{\circ}\text{C}$ due to physical activity or fever causes severe to profound deafness. In the five independent familial cases described so far, different missense mutations (Ile515Thr, Gly541Ser, Arg1607Trp and compound heterozygosity for Gly614Glu and Arg1080Pro) and an in-frame deletion (Glu1804del) were discovered (Varga *et al*, 2006; Romanos *et al*, 2009; Marlin *et al*, 2010; Wang *et al*, 2010; Matsunaga *et al*, 2012). Furthermore, three more missense mutations in otoferlin (Pro1987Arg, Glu1700Gln and Ile1573Thr) were described to cause moderate age-progressive hearing loss without evident temperature sensitivity (Varga *et al*, 2003; Chiu *et al*, 2010; Yildirim-Baylan *et al*, 2014). Unfortunately, speech perception, auditory temporal processing, auditory fatigue and temperature sensitivity have not been tested on these patients so far.

The severity of the hearing impairment of otoferlin mutant mouse lines studied to date (Roux *et al*, 2006; Longo-Guess *et al*, 2007; Pangrsic *et al*, 2010; Reisinger *et al*, 2011) has precluded further functional studies at the cellular, systems and behavioural level. To address this problem, we set out to generate a novel *Otof* mutant mouse model with an intermediate hearing defect, which would allow us to tackle current open questions regarding the function of otoferlin in synaptic sound encoding. We generated a knock-in mouse carrying the p.Ile515Thr point mutation (in NP_001274418), which was identified in one *OTOF* allele in siblings suffering from severe to profound hearing loss when their body temperature rises to $\geq 38.1^{\circ}\text{C}$ (Varga *et al*, 2006). At normal body temperature, patients had mild low-frequency hearing loss, speech comprehension below the 10th percentile both in quiet and noise and lacked ABRs. Later analysis revealed a premature STOP codon (Arg1116*) in the second *OTOF* allele (A. Starr, personal communication). The hearing disorder in *Otof*^{I515T/I515T} mice largely recapitulates the phenotype described in human patients, except for the temperature sensitivity. Comprehensive analyses of synaptic sound encoding in *Otof*^{I515T/I515T} mice from the molecular to the systems level indicate that otoferlin is critical for reformation of synaptic vesicles from endosome-like intermediates and for the replenishment of the RRP. Finally, we provide a candidate molecular mechanism for temperature-induced deafness in humans.

Results

The Ile515Thr mutation lowers otoferlin protein levels

We introduced the Ile515Thr substitution in mouse *Otof* via targeted knock-in (Appendix Supplementary Methods). First, we investigated the abundance and localization of otoferlin by using

immunohistochemistry and confocal fluorescence microscopy in organs of Corti of 14- to 15-day-old (P14–15) mice (Fig 1). Quantifying immunofluorescence per cell, we found a 65% reduction in otoferlin levels in *Otof*^{I515T/I515T} IHCs compared to wild-type (*Otof*^{+/+}) controls (Fig 1A, B and G). In a parallel analysis of *Otof*^{Pga/Pga} IHCs, a 69% reduction of protein levels was detected (Fig 1C and G), close to previous results (73%, Pangrsic *et al*, 2010). The reduction of otoferlin in the mutant genotypes was confirmed using another anti-otoferlin antibody (Appendix Fig S1A–D). The lower protein levels in *Otof*^{I515T/I515T} IHCs are likely due to a faster degradation of mutated otoferlin (Appendix Fig S1E). In *Otof*^{I515T/I515T} IHCs, the remaining otoferlin localized more towards the synaptic area below the midline of the nucleus of IHCs compared to *Otof*^{+/+}, while it was found more apically in *Otof*^{Pga/Pga} IHCs (Fig 1H). In the IHCs of all genotypes, otoferlin immunoreactivity was found in the cytoplasm and at the plasma membrane. In *Otof*^{I515T/I515T} IHCs, the otoferlin immunofluorescence at the plasma membrane relative to total cellular protein levels was unaltered as compared to *Otof*^{+/+} IHCs. In contrast, *Otof*^{Pga/Pga} IHCs showed an 85% lower relative membrane staining (Fig 1D–F and I). Taken together, the calculated absolute level of membrane-bound otoferlin was reduced by 66% in *Otof*^{I515T/I515T} and by 97% in *Otof*^{Pga/Pga} IHCs (Fig 1J).

We conclude that the Ile515Thr mutation lowers the absolute otoferlin levels, but preserves the relative distribution between plasma membrane and cytoplasm.

Auditory brainstem responses (ABRs) indicate a progressive hearing impairment in *Otof*^{I515T/I515T} mice

Hearing was first assessed by ABR recordings. ABR thresholds were elevated by 20 dB for pure tones and 10 dB for click stimuli in young *Otof*^{I515T/I515T} mice (Fig 2A). The amplitude of the spiral ganglion neuron (SGN) compound action potential, approximated as the amplitude of ABR wave I in response to clicks, was reduced to one-third of the *Otof*^{+/+} littermate values, while subsequent waves were better preserved (Figs 2B and C, and EV1A and B). Together, population responses indicate a mild impairment of synchronous auditory signalling already in juvenile mice. We then cross-bred *Otof*^{I515T/I515T} mice with deaf *Otof*^{-/-} mice in order to model the human *OTOF*^{I515T/R1116*} subjects (Varga *et al*, 2006) even more closely. We found an additional elevation of ABR thresholds by 15 dB and a further reduction of ABR amplitudes in *Otof*^{-/-I515T} mice, indicating a gene dosage-dependent effect (Figs 2A–C and EV1A). Consistent with a primary defect of the IHC synapse, distortion product otoacoustic emissions (DPOAE) were present, which report active cochlear amplification and require intact mechanoelectrical transduction (Fig EV1C).

Like in some patients with age-progressive hearing loss due to *OTOF* mutations (Varga *et al*, 2003; Chiu *et al*, 2010; Yildirim-Baylan *et al*, 2014), the hearing impairment, reflected by altered ABR thresholds and amplitudes, progressed rapidly during adolescence (Fig 2D–F), which correlated with a further reduction in otoferlin protein levels (Fig EV1D).

Intact synaptic vesicle fusion but impaired vesicle replenishment in *Otof*^{I515T/I515T} IHCs

Perturbations of otoferlin function have been shown to interfere with presynaptic function in IHCs (Roux *et al*, 2006; Pangrsic *et al*,

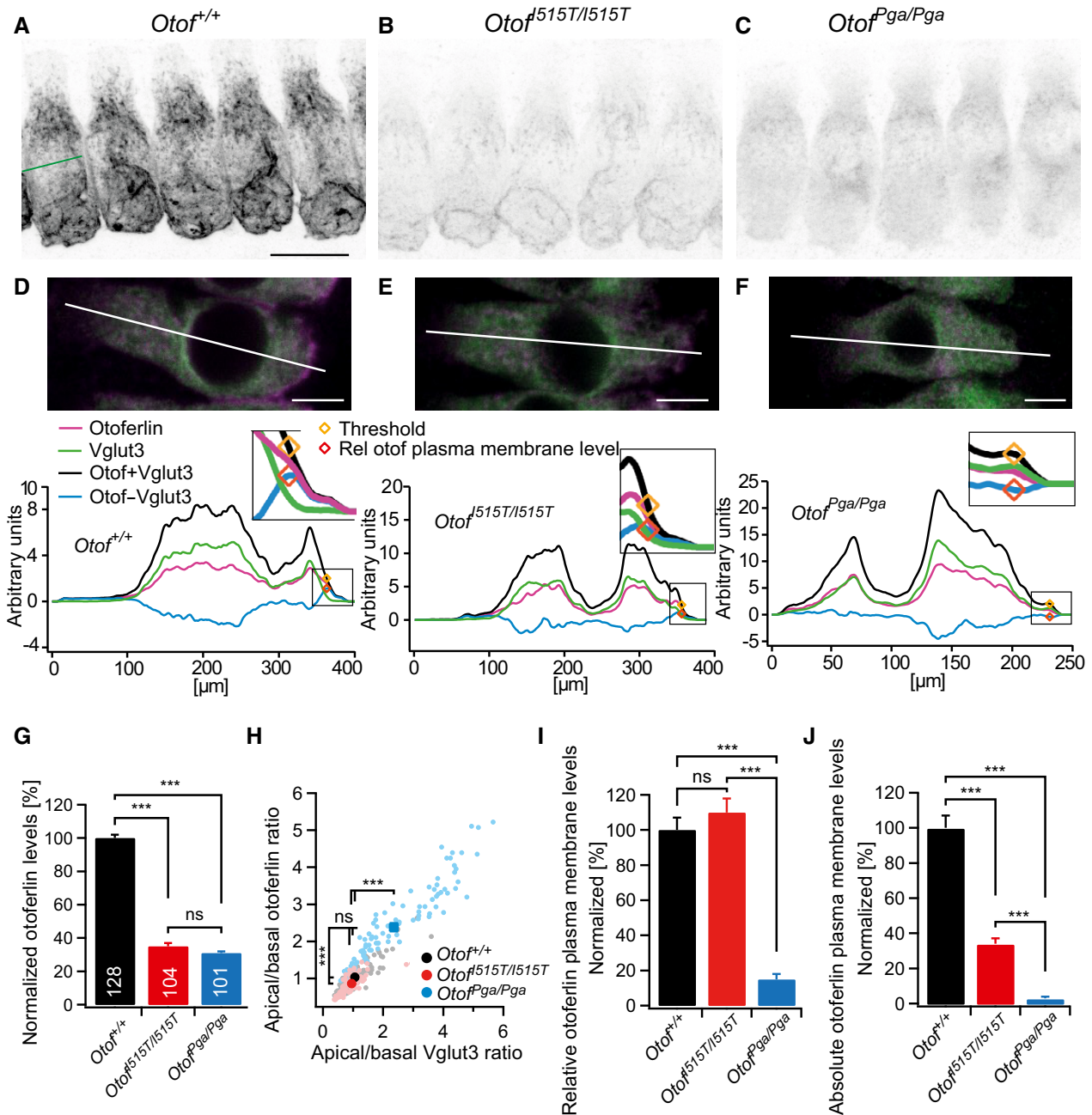


Figure 1. Otoferlin levels and cellular distribution are differentially affected in *Otof*^{I515T/I515T} and *Otof*^{Pga/Pga} IHCs.

A–C Immunofluorescence images (inverted intensity) of P14–P15 IHCs from indicated genotypes, revealing differences in otoferlin fluorescence intensity and distribution. Maximum projection of confocal stacks; scale bar, 10 μm.

D–F Upper panels, examples for IHCs, co-labelled for otoferlin (magenta) and Vglut3 (green) and position of the line for line scans; maximum projection of few optical sections; scale bars, 5 μm. Lower panels, for quantification of membrane staining, the fluorescence was normalized to the cellular fluorescence for each fluorophore, and then the average of five parallel line scans through the middle of the cells for the sum of both fluorescence values (black line) was used to determine the position of the basal membrane. At the most basal cellular point along this line which exceeds the threshold value of 2 (yellow diamond), the otoferlin-Vglut3 fluorescence difference (blue line) gave the value for relative otoferlin plasma membrane levels (orange diamond). Insets: enlargements of basal regions.

G Otoferlin protein levels were reduced in *Otof*^{I515T/I515T} IHCs (indicated numbers represent numbers of cells) and *Otof*^{Pga/Pga} IHCs compared to wild-type (*Otof*^{+/+}) controls (mean ± SEM).

H Ratio of apical/basal protein levels (above/below nuclear midline depicted as green line in (A)) indicates an apical shift of otoferlin in *Otof*^{Pga/Pga} IHCs.

I Relative levels of membrane-bound otoferlin at the basal pole of IHCs (mean ± SEM).

J Absolute amount of otoferlin at the basal IHC plasma membrane, gained by multiplication of relative plasma membrane levels (I) × total cellular otoferlin protein levels (G) (mean ± SEM).

Data information: Cell numbers in (G) apply also to (H–J); Kruskal–Wallis test; ****P* < 0.001.

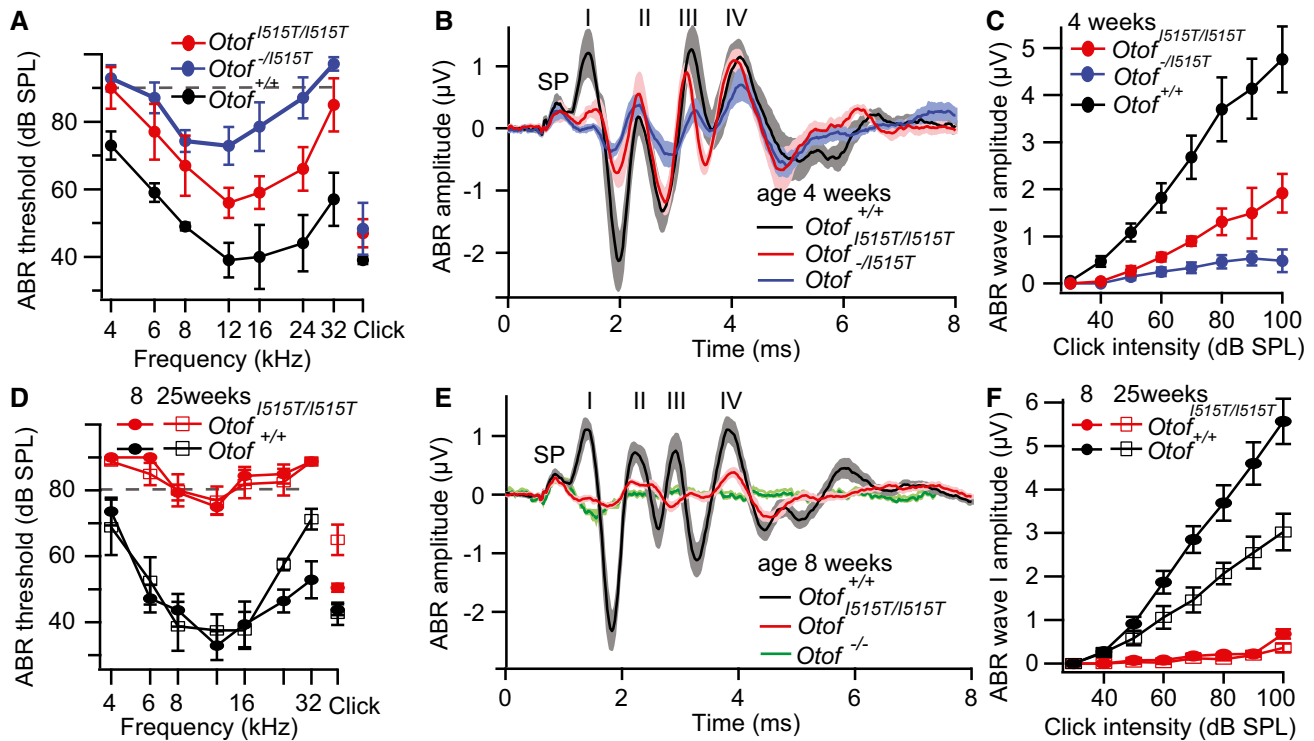


Figure 2. Hearing, assessed by ABR, is impaired due to the Ile515Thr mutation in otoferlin.

- A ABR thresholds in *Otof*^{I515T/I515T} (red, *n* = 5) and *Otof*^{-/-I515T} (blue, *n* = 7) mice were elevated compared to *Otof*^{+/+} mice (black, *n* = 5) at an age of 3–4 weeks. The grey dotted line indicates the maximum loudspeaker output of 90 dB; thresholds exceeding this value were set to 100 dB for calculation of the mean \pm SEM. At 12 kHz, only the threshold increase for *Otof*^{-/-I515T} versus *Otof*^{+/+} is significant (Kruskal–Wallis test with Dunn's multiple comparisons test between all three groups).
- B Grand averages of ABR waveforms \pm SEM in response to 80 dB click stimulation of the mice analysed in (A): The small wave preceding ABR wave I probably represents the summating potential (SP, hair cell receptor potential), which is intact in *Otof* mutants. ABR wave I is reduced in amplitude while subsequent peaks are better preserved in *Otof*^{I515T/I515T} mice (Fig EV1).
- C Mean ABR wave I amplitude \pm SEM for different stimulus intensities (all differences between genotypes are significant; two-way ANOVA with Tukey's multiple comparison test).
- D At 8 weeks (circles) and 25 weeks (open squares), *Otof*^{I515T/I515T} mice showed highly elevated ABR thresholds compared to *Otof*^{+/+} mice (*n* = 7–8 each; *P* < 0.001 at 12 kHz, Mann–Whitney *U*-test). Grey dotted line as in (A).
- E Grand averages of ABR waveforms \pm SEM in response to 80 dB click stimulation in mice aged 8 weeks. *Otof*^{I515T/I515T} (*n* = 8) have drastically reduced ABR amplitudes compared to *Otof*^{+/+} mice (*n* = 7). *Otof*^{-/-} mice have no ABR (green, *n* = 9).
- F Mean ABR wave I amplitude \pm SEM for different stimulus intensities for 8-week-old and 25-week-old *Otof*^{I515T/I515T} and *Otof*^{+/+} mice (*P* < 0.001, two-way ANOVA).

2010). To test the effect of the Ile515Thr mutation, we performed perforated-patch recordings from IHCs in P14–P17 mice at room temperature (RT). The current–voltage relationship revealed a normal voltage dependence of activation and amplitude of Ca^{2+} currents in *Otof*^{I515T/I515T} IHCs (Fig 3A and B). We then measured exocytosis as increments of plasma membrane capacitance (ΔC_m) in response to step depolarizations to the voltage where maximal Ca^{2+} currents are elicited (typically -14 mV). Depolarizations were followed by recovery periods of 30 to 60 s at -84 mV, which precludes exocytosis triggered by voltage-gated Ca^{2+} influx. Comparable ΔC_m in response to short depolarizations (2–20 ms) indicated intact fusion of a normally sized RRP under these experimental conditions (Fig 3C and D). Consistently, the number of ribbon synapses was normal in mutant IHCs (Fig EV1E and F). However, when *Otof*^{I515T/I515T} IHCs were depolarized for 50 ms or longer, exocytosis was significantly smaller than in controls (Fig 3C and D). Such sustained exocytosis is thought to reflect replenishment of synaptic vesicles to the RRP and their subsequent fusion, and/or active zone clearance (Pangršić *et al*, 2012). The rate of sustained

exocytosis was reduced to ~ 340 vesicles/s/active zone, compared to ~ 700 vesicles/s/active zone in *Otof*^{+/+} IHCs (see Appendix Supplementary Methods), but was still considerably faster than in *Otof*^{Pga/Pga} IHCs (~ 200 vesicles/s/active zone, Pangršić *et al*, 2010).

In order to test the fusion kinetics of RRP vesicles in *Otof*^{I515T/I515T} IHCs, we recorded ΔC_m in response to fast Ca^{2+} uncaging by UV laser. Here, exocytosis was comparable in kinetics between *Otof*^{I515T/I515T} and *Otof*^{+/+}. The amplitude was significantly reduced in *Otof*^{I515T/I515T} IHCs (Fig 3E and F; fast and slow components reduced to 40 and 63%, respectively). This indicates that the Ile515Thr mutation does not impair the Ca^{2+} -triggered fusion of vesicles to the plasma membrane itself, but instead impairs vesicle replenishment, potentially affecting priming, active zone clearance or yet another mechanism.

***In vivo* postsynaptic recordings reveal a use-dependent depression of sound encoding at *Otof*^{I515T/I515T} synapses**

In order to directly assess sound encoding at *Otof*^{I515T/I515T} synapses *in vivo*, we performed extracellular recordings from individual SGNs,

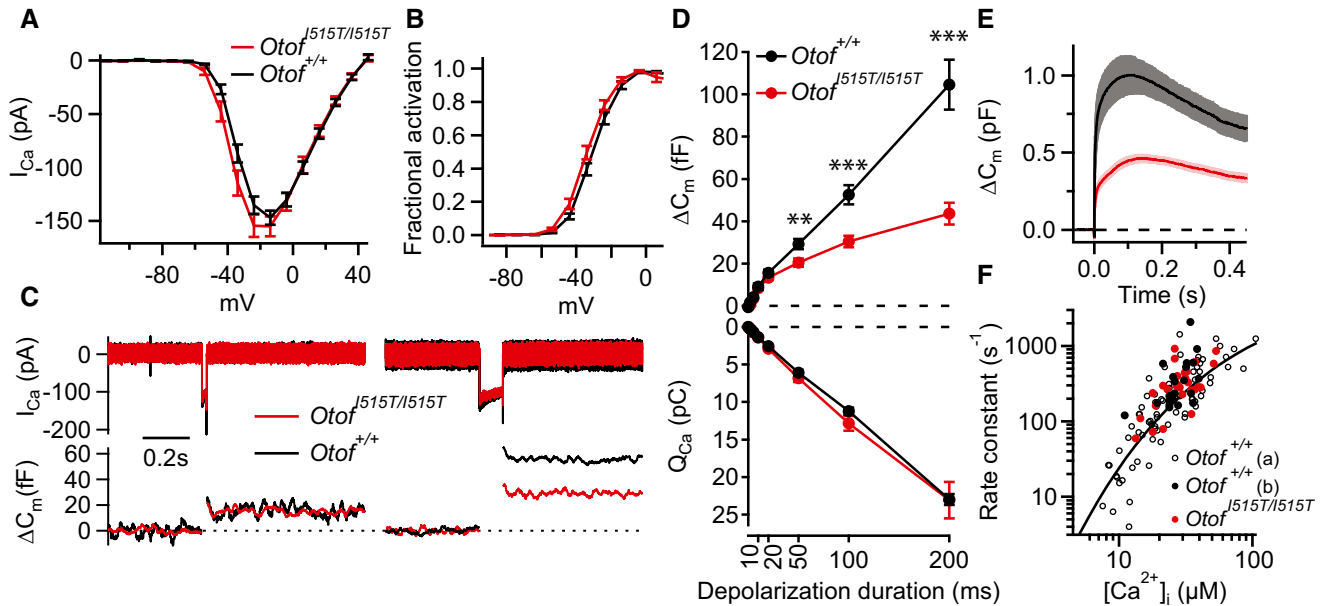


Figure 3. Sustained exocytosis is impaired in *Oto^f^{I515T/I515T}* hair cells.

- A, B No difference in voltage-dependent Ca^{2+} currents (A) and fractional activation of I_{Ca} channels (B) between *Oto^f^{I515T/I515T}* IHCs ($n = 16$) and IHCs of *Oto^f^{+/+}* littermates ($n = 13$; mean \pm SEM).
- C Exocytosis was recorded by measures of changes in membrane capacitance (ΔC_m , lower panel) in response to depolarization (left, 20 ms; right, 100 ms) to the voltage where maximum Ca^{2+} currents were elicited (upper panel), typically -14 mV. Representative examples.
- D Upper panel, while for stimuli up to 20 ms exocytosis from *Oto^f^{I515T/I515T}* ($n = 13$) and *Oto^f^{+/+}* ($n = 11$) IHCs was similar, sustained exocytosis, representing most likely the release of replenished vesicles, was significantly reduced in *Oto^f^{I515T/I515T}* IHCs (mean \pm SEM; t-test; ** $P < 0.01$; *** $P < 0.001$). Lower panel, Ca^{2+} current integrals were of similar size (mean \pm SEM).
- E Flash photolysis of caged Ca^{2+} elicited a smaller exocytic response in *Oto^f^{I515T/I515T}* IHCs (mean \pm SEM).
- F The kinetics of the fast component from (E) was comparable between *Oto^f^{I515T/I515T}* IHCs and *Oto^f^{+/+}* littermates (black circles). Open circles represent previously published data on IHCs of hearing wild-type mice (Beutner et al, 2001; Pangrsic et al, 2010).

each driven by a single IHC active zone (Fig 4). We found spontaneous spiking (Fig 4A), sound thresholds and frequency tuning (Fig EV2A and B) of individual SGNs to be normal which corroborates our notion of intact cochlear amplification in *Oto^f^{I515T/I515T}* mice. Upon stimulation with tone bursts at a stimulus rate of 2 Hz, *Oto^f^{I515T/I515T}* SGNs showed a near-normal onset response with a high rate of instantaneous spiking, but then underwent stronger spike rate adaptation, not reaching a steady state within the 50 ms of stimulation (Fig 4B and E; ratio of onset/adapted rates 5.2 ± 1.8 in *Oto^f^{I515T/I515T}* SGNs versus 3.5 ± 0.2 in *Oto^f^{+/+}* SGNs, $P = 0.03$, t-test). Compared to SGNs from *Oto^f^{+/+}* littermates, the time course of adaptation was slower (Tau 10.9 ± 3.0 ms versus 6.1 ± 1.7 ms, single exponential fit, $P < 0.001$, t-test).

At higher stimulus rates of 5 or 10 Hz, both onset and adapted spike rates decreased dramatically (Fig 4C–E). Consistent with the reduced spiking at sound onset, the first spikes then also showed a highly significant increase in latency (Fig EV2C) and jitter (Fig 4F). As evoked spike rates were low and the dynamic range unchanged, rate-intensity functions of individual SGNs were shallower than normal (Figs 4G and EV2D and E). The spike rates and precision of spike timing were even further decreased when continuous amplitude-modulated sound stimuli were applied (Figs 4G and H, and EV2F). The enhanced adaptation and slowed recovery from adaptation were also obvious from responses to paired stimuli (Fig 4I) where the half-time of recovery from forward masking was fivefold increased from 28.7 ± 5.6 ms in 9

Oto^f^{+/+} to 157.5 ± 40.5 ms in 13 *Oto^f^{I515T/I515T}* SGNs ($P < 0.001$, Mann–Whitney U-test). In summary, *Oto^f^{I515T/I515T}* SGNs show an unusual sound encoding deficit that is dominated by a use-dependent reduction of sound-evoked spiking, likely resulting from impaired replenishment of the RRP and/or impaired active zone clearance.

Impaired synaptic sound encoding in *Oto^f^{I515T/I515T}* mice affects the perception of silent gaps in noise

Using prepulse inhibition of the acoustic startle response, we found an impairment of gap detection performance in *Oto^f^{I515T/I515T}* mutants compared to *Oto^f^{+/+}* littermates (Fig EV3A–C). We propose that this is consistent with the delayed recovery from adaptation (Fig 4I) and reflects the impaired vesicle replenishment during the gap. For a more sensitive method that approaches the physiological limit of gap detection abilities, we then employed operant conditioning using the Audiobox system (de Hoz & Nelken, 2014). We conditioned mice to attempt to drink water only when continuous broadband noise was present. When the noise was interrupted by 90 ms silent gaps, access to the water bottles was denied and drink attempts were punished by air puffs. After reaching $> 30\%$ discrimination performance, we introduced shorter gaps in a total of 8% of the trials. The two *Oto^f^{+/+}* mice avoided drinking when gaps lasted 3 ms or more. This agrees well with descriptions of gap thresholds near 2 ms in CBA/J mice (Radziwon et al, 2009).

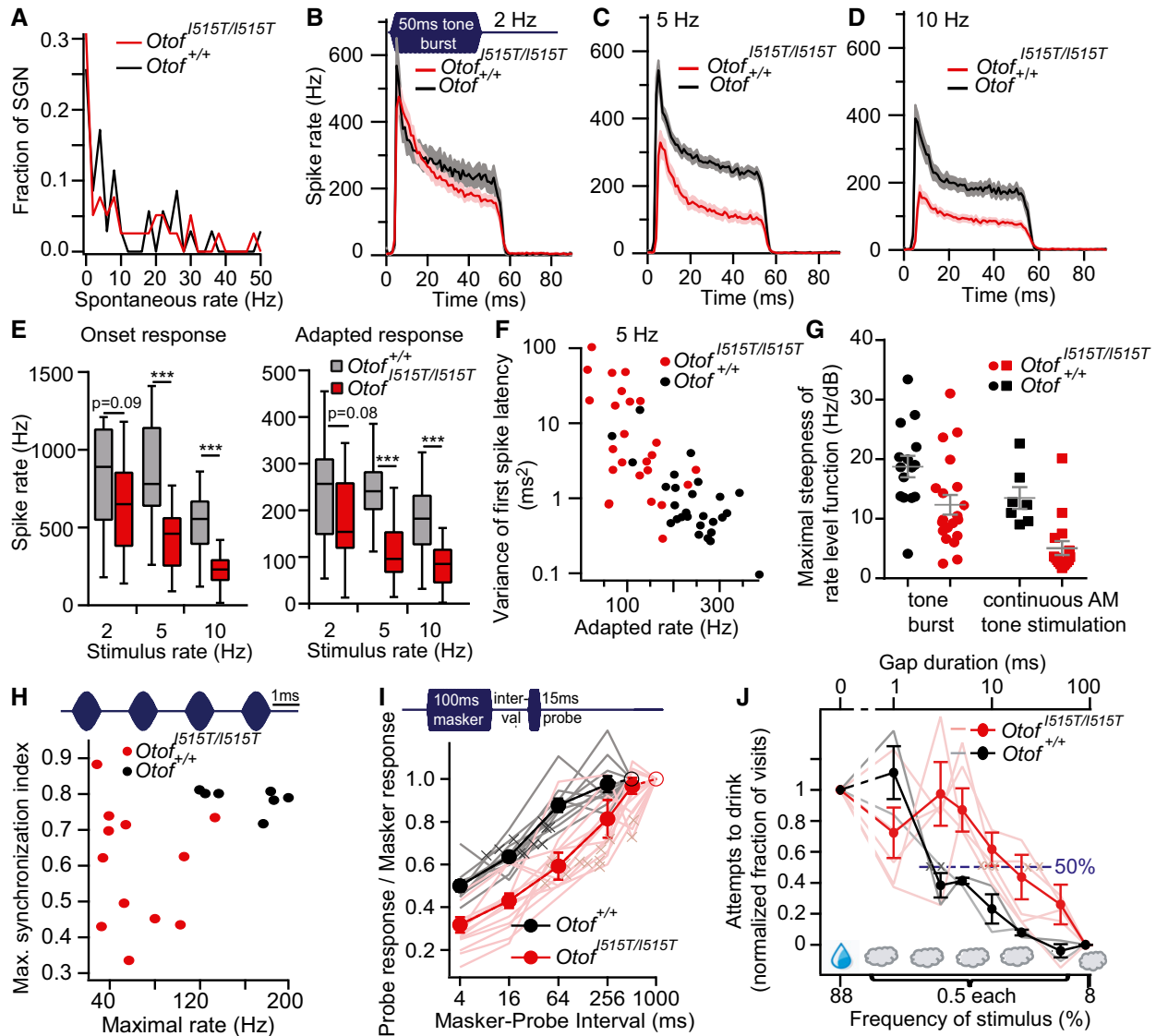


Figure 4. Enhanced adaptation and slowed recovery of SGN spiking in *Otof*^{I515T/I515T}.

- A** Spontaneous rates of SGNs from *Otof*^{I515T/I515T} (red, *n* = 35) and *Otof*^{+/+} littermates (black, *n* = 39) were not significantly different (*P* = 0.83, Kolmogorov–Smirnov test).
- B–D** Averaged poststimulus time histograms ± SEM from *Otof*^{I515T/I515T} mice (*n* = 25–32) and *Otof*^{+/+} littermate SGNs (*n* = 13–27) to stimulation with 50 ms tone bursts at the characteristic frequency (CF) of each fibre, 30 dB above threshold at indicated stimulus rates.
- E** Quantification of onset (largest 0.5 ms bin, Mann–Whitney *U*-test) and adapted responses (averaged 35–45 ms from response onset, ****P* < 0.001, *t*-test, Tukey quartile box plot) from data in (B–D).
- F** The jitter of the first sound-evoked spike was significantly increased (*P* < 0.001, Mann–Whitney *U*-test) but retained its inverse correlation with spike rates.
- G** Spike rate increases with rising stimulus intensity were significantly shallower in *Otof*^{I515T/I515T} SGNs, both for repetitive stimulation with 50 ms tone bursts (left, *P* = 0.014, *t*-test) and for continuous stimulation with amplitude-modulated tones (right, *P* < 0.001, Mann–Whitney *U*-test). Lines represent mean ± SEM.
- H** Phase locking to amplitude-modulated tones (assessed as the maximal synchronization index) was typically less precise in *Otof*^{I515T/I515T} SGNs than in *Otof*^{+/+} SGNs (*P* = 0.09, Mann–Whitney *U*-test).
- I** 100 ms masker tone and 15 ms probe tones (both at CF, 30 dB above threshold) were separated by silent intervals of variable duration. Inter-masker intervals were 500 ms for *Otof*^{+/+} and 1,000 ms for *Otof*^{I515T/I515T}. The ratio of probe and masker onset responses revealed enhanced RRP depletion after stimulation in *Otof*^{I515T/I515T} (pink; mean ± SEM red) compared to *Otof*^{+/+} (grey; mean ± SEM black; for 4 ms interval: *P* = 0.001, *t*-test) and a slowed time course of recovery (x: half-time of recovery, interpolated from normalized recovery functions; *P* < 0.001, Mann–Whitney *U*-test).
- J** Mice learned to drink water when continuous noise was present but avoided drinking when the noise was interrupted by silent gaps. 5 *Otof*^{I515T/I515T} mice (pink, mean ± SEM red) avoided drinking less efficiently than 2 *Otof*^{+/+} mice (grey, mean ± SEM black) for shorter gap durations. See also Fig EV3.

In contrast, *Otof*^{I515T/I515T} often attempted to drink in trials with short gaps (Figs 4J and EV3F). The interpolated 50% value of the normalized discrimination function was 2.7 ± 0.4 ms in *Otof*^{+/+} mice and 17.2 ± 4.9 ms in *Otof*^{I515T/I515T}.

In a second task, we conditioned mice to avoid drinking when they heard 12 kHz tone bursts. The responses to varying tone intensities indicate comparable hearing thresholds in two *Otof*^{I515T/I515T} mice and one *Otof*^{+/+} mouse (Fig EV3D and E).

Together, the impaired gap detection performance and normal sound sensitivity in *Otof*^{I515T/I515T} mice are consistent with the results of *in vivo* recordings from SGNs that show normal sound sensitivity but impaired recovery from adaptation. Like in other mice with synaptic transmission deficits (e.g. Buran *et al*, 2010; Jung *et al*, 2015) and patients with auditory synaptopathy/neuropathy, the deficit appears overly pronounced in ABR recordings which represent a combination of the sensitivity, the rate and the synchronicity of SGN firing.

ABR amplitudes gradually decline at elevated temperature

Our data show that *Otof*^{I515T/I515T} mice reflect the auditory phenotype of human patients at normal body temperature very well. Thus, we assume that the synaptic disease mechanisms found in mice at or below physiological temperature likely describe the situation in human patients. We next assayed whether mice, like the human patients, experience an exacerbation of their hearing loss when their body temperature exceeds 38°C (Varga *et al*, 2006). We monitored the amplitude of ABR wave I in response to click stimulation while locally applying heat to the inner ear (Fig 5A–C and Appendix Fig S2). Here, we found a reversible linear decrease in ABR wave I amplitude in both *Otof*^{I515T/I515T} and *Otof*^{+/+} littermate mice, with comparable average regression slopes of 0.084 $\mu\text{V}/^\circ\text{C}$ and 0.081 $\mu\text{V}/^\circ\text{C}$, respectively. The effect varied considerably between animals, presumably due to variable experimental conditions. In some animals (3/6 *Otof*^{I515T/I515T} and 2/6 *Otof*^{+/+}), ABR amplitudes did not recover after extensive heating (Appendix Fig S2B and C), presumably indicating permanent heat damage. Nonetheless, since ABRs in the mouse model never disappeared completely, we conclude that the elevated cochlear temperature did not fully abolish sound encoding in *Otof*^{I515T/I515T} mouse mutants, as it seems to be the case in human *Otof*^{I515T/R1116*} patients. Thus, as the heat-induced phenotype seems to be weaker in mice compared to human patients, the cell physiological or ultrastructural effect of fever found in our mouse model might also be weaker than in human patients.

A 20 amino acid stretch present in human otoferlin reduces plasma membrane localization of Ile515Thr-otoferlin

Looking at differences in the protein sequence of human and mouse otoferlin which might contribute to the less pronounced heat sensitivity in mice, we found an arginine-rich insertion including an RXR motif at position 1244–1263 in the long human reference sequences (e.g. variant e; NP_001274418). While there is currently no experimental evidence which splice isoform regarding this motif is expressed in human IHCs, PCRs on mouse organ of Corti cDNA revealed that the isoform lacking this RXR motif is predominant in mouse IHCs (Fig EV4). A similar motif was described to cause a temperature-dependent decrease in surface expression of an alpha-adrenergic receptor (Filipeanu *et al*, 2011, 2015). We subcloned the human RXR stretch into mouse otoferlin cDNA and performed biolistic transfection into *Otof*^{-/-} IHCs (Fig 5E–I). RXR-otoferlin showed a strong plasma membrane immunostaining (relative to total cellular otoferlin levels), which was comparable to the values from explanted *Otof*^{+/+} cells

(Fig 5D and J). Otoferlin with both the Ile515Thr mutation and the RXR motif, however, displayed almost complete absence from the plasma membrane already at 37°C (Fig 5H–J), which is in stark contrast to mouse Ile515Thr-otoferlin (Fig 1). Since the abundance of otoferlin at the plasma membrane seems to be most relevant for sound encoding *in vivo*, this might explain the more pronounced heat sensitivity in human patients. When comparing to the hearing phenotype of our mouse models, hearing at normal and elevated temperature in human Ile515Thr patients would best be explained by a mixture of the splice variant with RXR and the splice variant without being expressed in human IHCs.

Heat reduces exocytosis and otoferlin membrane levels

We next tested for a synaptic dysfunction elicited by fever by performing patch clamp recordings of IHCs (Fig 6). We recorded ΔC_m in IHCs induced by 5–100 ms depolarization steps, first at room temperature (RT), then at near physiological temperature (PT, 35–36.5°C), followed by high temperature (38.5–40°C). Consistent with a previous study (Nouvian, 2007), we found Ca^{2+} currents and exocytosis from *Otof*^{+/+} IHCs to increase when temperature was raised from RT to PT (Fig 6A and B). While Ca^{2+} current integrals increased only by 27 and 15% in *Otof*^{+/+} ($n = 4$) and *Otof*^{I515T/I515T} ($n = 5$), respectively, exocytosis was more strongly enhanced by warming (Fig 6B) and increased 2.7- to threefold in both genotypes.

We next heated the bath to 38.5–40°C expecting a strong reduction of exocytosis for *Otof*^{I515T/I515T} IHCs given the human fever-induced deafness. Recordings were started as soon as the temperature recorded in the bath close to the tissue was stable. Surprisingly, we found a strong decline in ΔC_m for *Otof*^{+/+} IHCs compared to PT, especially for sustained exocytosis which was halved (Fig 6C and F). This fever-induced reduction was weaker in *Otof*^{I515T/I515T} (13% less than at PT; Fig 6G). As a result, ΔC_m did not differ between *Otof*^{I515T/I515T} and *Otof*^{+/+} IHCs at high temperature for all depolarization durations tested (Fig 6C). However, we cannot exclude that a longer heating period might have unravelled a stronger synaptic dysfunction in *Otof*^{I515T/I515T} IHCs. In fact, sustained exocytosis between the genotypes appeared slightly stronger in recordings after heating. At 2 min of recovery at $< 29^\circ\text{C}$, exocytosis in *Otof*^{+/+} IHCs was reduced to 52% relative to RT before heating for depolarization stimuli of ≥ 10 ms ($n = 4$), while in *Otof*^{I515T/I515T} IHCs, it was reduced to 40% of initial RT values ($n = 3$; Fig 6D, F and G). Ca^{2+} currents were of similar size as before heating and comparable between *Otof*^{+/+} and *Otof*^{I515T/I515T} IHCs. In few of these IHCs, exocytosis was tested also after a longer recovery period of 5–20 min, and we recorded additional cells only after heating (Fig 6E). Considering IHCs of both conditions, we found ΔC_m levels for 100 ms depolarization in *Otof*^{+/+} IHCs to be restored to 61% compared to observations at RT before heating ($n = 7$ from 4 cells). In contrast, in *Otof*^{I515T/I515T} IHCs, sustained exocytosis remained reduced (37% of initial values for 100 ms depolarization, $n = 8$ from 4 cells).

Based on the loss of exocytic capacity in wild-type and mutant IHCs between PT and $\geq 38.5^\circ\text{C}$, we propose that part of the synaptic machinery is thermally unstable. The poorer recovery from heat in *Otof*^{I515T/I515T} IHCs and the temperature-sensitive phenotype of patients with different OTOF mutations suggest that otoferlin itself

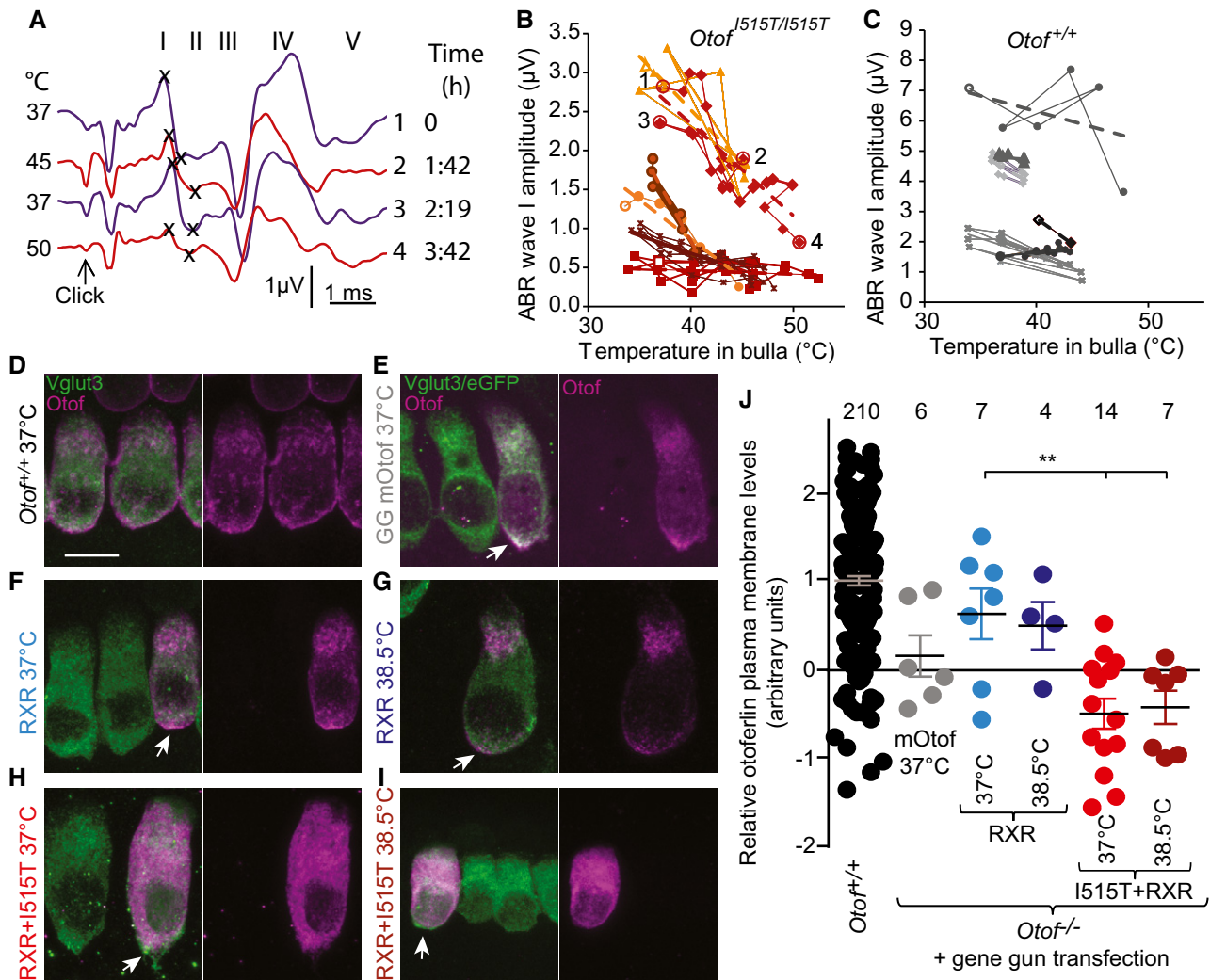


Figure 5. Apparently lower thermal sensitivity of hearing in mice than in humans, likely due to a human RXR motif reducing plasma membrane localization of Ile515Thr-otoferlin.

A Exemplary ABR traces (click 100 dB) from one *Otof*^{I515T/I515T} mouse recorded at indicated bulla temperatures during local heating. Note that ABRs never disappeared completely, but wave I amplitude changed reversibly with temperature.

B, C ABR wave I amplitudes in *Otof*^{I515T/I515T} (B, click 100 dB) and *Otof*^{+/+} mice (C, click 80 dB) decreased with increasing temperature in the bulla. Each colour represents a different experiment, and dashed lines are line fits. Open symbols indicate the beginning of the experiments; subsequent recordings are connected by lines. The four indicated data points in (B) correspond to ABRs in (A).

D Explanted organ of Corti from an *Otof*^{+/+} mouse at P4 after 2 days *in vitro* (DIV2) at 37°C immunostained against otoferlin (magenta) and Vglut3 (green). Note the intense immunostaining of otoferlin at the plasma membrane. Scale bar, 10 μm.

E–I Explanted organs of Corti from *Otof*^{-/-} mice at P4 were transfected by GeneGun with otoferlin cDNA and eGFP and immunostained at DIV2. (E) Example cell transfected with wild-type mouse otoferlin cDNA. (F, G) Representative cells transfected with mouse otoferlin including the 20 amino acids of the RXR motif (see Fig EV4). Cells in (G) were incubated at 38.5°C for 30 min prior to fixation. The RXR-otoferlin transfected cells (F, G) show a membrane localization of otoferlin surrounding the Vglut3 immunofluorescence/eGFP fluorescence at the basal pole of the cells (arrows), similar as in controls (D, E). (H, I) Both the human RXR motif and the Ile515Thr mutation were introduced in mouse cDNA, and cells were incubated at 37°C (H) or for 30 min at 38.5°C (I) before fixation. Here, green fluorescence surrounds the otoferlin immunofluorescence (arrows), suggesting loss of otoferlin from the plasma membrane.

J Quantification of the relative plasma membrane levels of otoferlin (as in Fig 1) revealed normal plasma membrane abundance when the human RXR motif was present, but a strong reduction for otoferlin with RXR and Ile515Thr (individual cells; mean ± SEM; t-test; ***P* < 0.01).

is the heat-sensitive protein and that heat instability of otoferlin is enhanced by certain mutations like Ile515Thr.

Indeed, 3D structure predictions show that the isoleucine 515 points towards the hydrophobic core of the C₂C domain (Appendix Fig S3), suggesting that an exchange into the more hydrophilic threonine potentially decreases the stability of the protein. Since we also did not find a change in otoferlin mRNA

levels in *Otof*^{I515T/I515T} organs of Corti, ruling out lower transcription levels or destabilized mRNA as a cause (Appendix Fig S4A), we hypothesized that mutations in otoferlin lead to faster protein degradation at elevated temperature. Testing the degradation rate of a series of otoferlin mutants related to human heat-induced deafness after heterologous expression in HEK293T cells, we found hardly any degradation within 2 or 24 h even at elevated temperature,

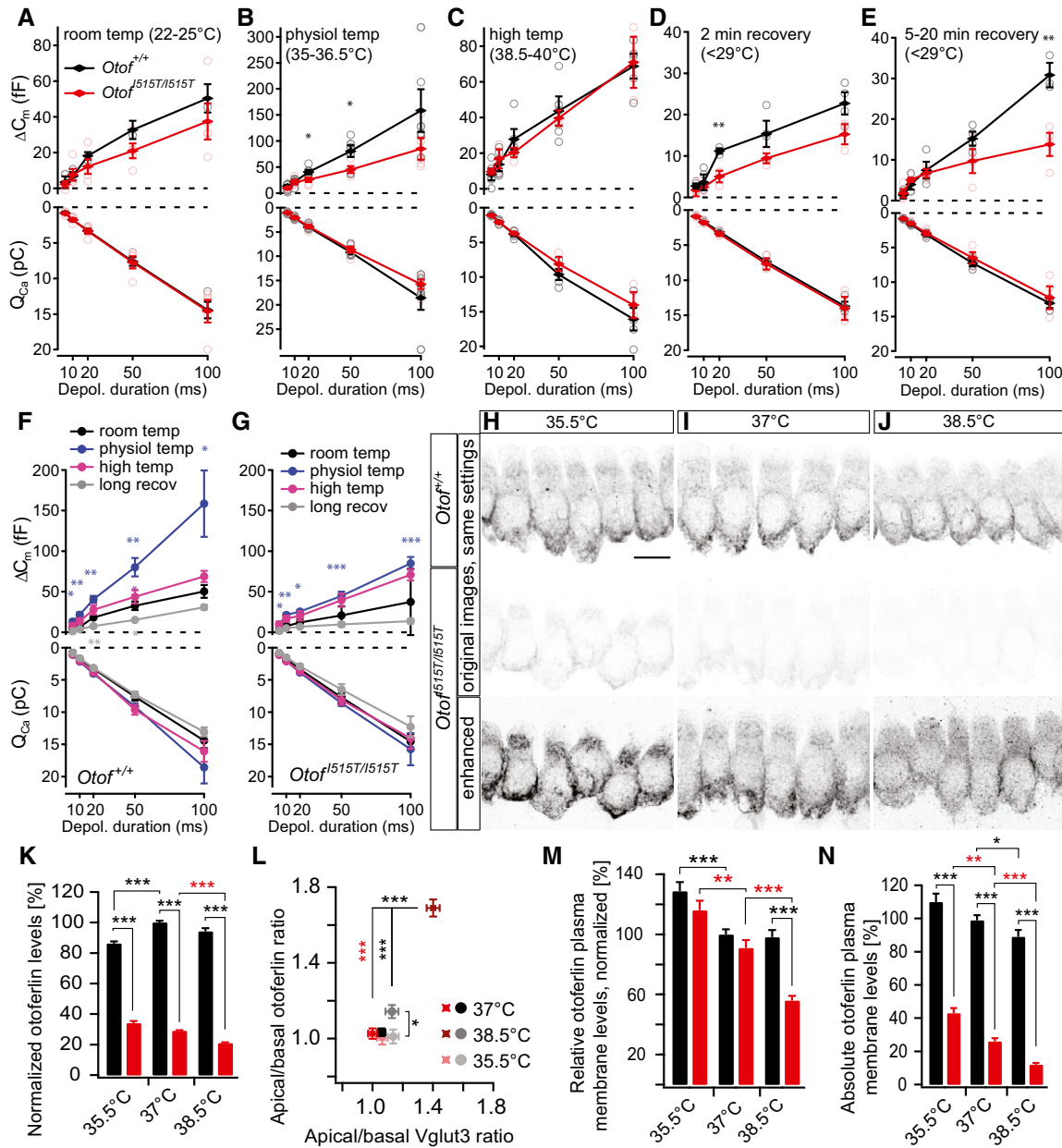


Figure 6. Temperature alters exocytosis, otoferlin protein levels and plasma membrane abundance.

A–E Capacitance increments recorded from *Otof*^{+/+} (black) and *Otof*^{I515T/I515T} (red) IHCs. Individual cells recorded at indicated temperatures (light circles), mean ± SEM (filled circles) for perforated-patch clamp experiments.

F, G Summary of the capacitance changes and Ca²⁺ current integrals for *Otof*^{+/+} (**F**) and *Otof*^{I515T/I515T} IHCs (**G**) at the different temperatures illustrates the drastic increase in exocytosis for physiological temperature. Significant differences compared to RT measurements are indicated with colours of the respective temperature, and between PT and high temperature in violet.

H–J Otoferlin immunofluorescence in *Otof*^{+/+} IHCs (upper panel) and *Otof*^{I515T/I515T} IHCs (middle and lower panels) of explanted organs of Corti at P7–P8 after incubation at indicated temperatures for 24 h; maximum projections of z-stacks, inverted images; scale bar, 10 μm. The same imaging settings have been applied in all experiments, and the same lookup table was applied for the upper and middle panels. Images of lower panels are enhanced compared to middle panels (lookup table covering full data range of only this genotype) to visualize otoferlin distribution.

K Quantification of otoferlin immunofluorescence in *Otof*^{+/+} IHCs (black bars) and *Otof*^{I515T/I515T} IHCs (red bars) indicates reduced protein levels with increasing temperature.

L Apical/basal otoferlin protein distribution, revealing a significant apical shift of otoferlin and Vglut3 for *Otof*^{I515T/I515T} IHCs (red symbols) at 38.5°C compared to *Otof*^{+/+} (grey/black symbols).

M Relative levels of membrane-bound otoferlin were lowered with increasing temperature.

N Absolute otoferlin membrane immunostaining strongly decreased with temperature.

Data information: All data presented are mean ± SEM. *n* = 98–137 *Otof*^{+/+} cells and *n* = 90–97 *Otof*^{I515T/I515T} cells in (**K–N**), 4–5 experiments. *t*-test (**A–G**) or Kruskal–Wallis test (**K–N**); **P* < 0.05; ***P* < 0.01; ****P* < 0.001.

similar as for wild-type otoferlin (Appendix Fig S4B and C). Although the lifetime of mutated otoferlin might be shorter in IHCs (see Appendix Fig S1E), the degradation seems too slow to explain hearing loss due to elevation of the body temperature. We hypothesize that loss of otoferlin from the plasma membrane in addition to protein unfolding might explain acute IHC presynaptic dysfunction at fever.

Next, we tested steady-state levels and subcellular distribution of otoferlin after prolonged incubation at elevated temperature (Fig 6H–J). In cultures of P7–8 organs of Corti incubated for 24 h at 37°C, the physiological temperature of mice (<http://www.informatics.jax.org>), otoferlin protein levels in *Otof*^{I515T/I515T} IHCs were reduced to 29% of *Otof*^{+/+} controls at 37°C (Fig 6K). After 24-h incubation at 38.5°C, otoferlin protein levels were even further reduced to 21%, and, remarkably, both otoferlin and Vglut3 localized more apically in *Otof*^{I515T/I515T} IHCs (Fig 6L), resembling the distribution found in *Otof*^{Pga/Pga} IHCs (Fig 1H). The relative levels of plasma membrane-bound otoferlin were strongly reduced at febrile temperature (56% of controls, Fig 6M), resulting in a strong temperature-dependent reduction of the absolute amount of plasma membrane-bound otoferlin in *Otof*^{I515T/I515T} IHCs (12% of controls, Fig 6N).

In summary, otoferlin is sensitive to heat, which is exacerbated by mutations like Ile515Thr. We found indications for faster degradation and loss from the plasma membrane of Ile515Thr-otoferlin at febrile temperature.

Otoferlin is localized at the plasma membrane and at endosomal vesicles, and synaptic vesicles are enlarged in *Otof*^{I515T/I515T} IHCs

Next, we analysed the subcellular distribution of otoferlin at the ultrastructural level by performing pre-embedding immunogold labelling and electron microscopy (EM) of P15–P16 IHCs (Fig 7 and Appendix Fig S5). The near absence of gold clusters in *Otof*^{−/−} tissue confirmed specificity of immunogold labelling (Fig 7C). In both *Otof*^{+/+} and *Otof*^{I515T/I515T} IHCs, otoferlin immunogold signal was present at the plasma membrane including the active zone

membrane (Fig 7A, B and D–G, and Appendix Fig S5), and at vesicular structures, some of which exhibited clathrin-coated vesicle budding (Fig 7I and J) indicating endosomal nature. The diameter of labelled intracellular membranous structures was, on average, larger in *Otof*^{I515T/I515T} (210 ± 13 nm; smallest diameter: 51 nm; *n* = 86) than in *Otof*^{+/+} IHCs (151 ± 8 nm, smallest 52 nm; *n* = 82, *P* < 0.001; Fig 7K) and thus clearly exceeded the typical synaptic vesicle diameter in IHCs (Chapochnikov *et al*, 2014). Hardly any otoferlin labelling was visible in < 100 nm distance to the ribbons where a halo of synaptic vesicles resides, neither in *Otof*^{+/+} nor in *Otof*^{I515T/I515T} IHCs, using two different pre-embedding protocols (Fig 7D–G). This discrepancy to earlier immunogold studies reporting a synaptic vesicle localization of otoferlin (Roux *et al*, 2006) might be due to pre- versus postembedding protocols used and/or different primary antibodies and a potential masking of our antibody epitope specifically at synaptic vesicles. In contrast, immunogold labelling for the vesicular glutamate transporter Vglut3 resulted in a strong signal around the ribbon (Fig 7H and Appendix Fig S5). Quantification of the gold particles revealed an overall reduction of otoferlin labelling in the cytoplasm and a strong trend towards lower levels at the membrane in *Otof*^{I515T/I515T} hair cells (Fig 7L and M), consistent with our immunofluorescence results. We conclude that the Ile515Thr mutation does not alter the subcellular distribution of otoferlin.

The larger average diameter of otoferlin-labelled structures in *Otof*^{I515T/I515T} IHCs might point towards impaired membrane turnover. We thus assessed the effects of the Ile515Thr mutation on synaptic ultrastructure and vesicle pool dynamics at 36 and 39°C by performing transmission EM of IHC ribbon synapses following inhibition or stimulation of exocytosis and subsequent chemical fixation. To inhibit IHC exocytosis, isolated organs of Corti were incubated in Ca²⁺-free saline, while stimulation employed extracellular saline with 1.3 mM Ca²⁺ and 40 mM K⁺ (according to the Nernst equation depolarizing IHCs to ~−30 mV). We found the number of membrane-proximal and ribbon-associated vesicles quantified in random ultrathin sections to be similar in all four conditions (stimulatory and inhibitory at 36/39°C) and both

Figure 7. The Ile515Thr mutation does not affect the subcellular localization of otoferlin but alters the size of endosomal and synaptic vesicles.

- A–C Pre-embedding immunogold labelling for EM visualizes otoferlin localization in random ultrathin sections through the basal part of IHCs in *Otof*^{+/+} (A) and *Otof*^{I515T/I515T} (B) but not in *Otof*^{−/−} (C) mice. IHCs are highlighted in beige. Scale bar, 200 nm.
- D–G Magnified synaptic ribbons (R) and postsynaptic afferent boutons of SGNs (Aff), displaying otoferlin immunogold labelling at active zone membranes (pink arrowheads) but not around the synaptic ribbon, using saponin permeabilization (D–F), or Triton X-100 treatment (G). Scale bar, 100 nm.
- H Vglut3 immunogold labelling adjacent to the ribbon as expected for a synaptic vesicle protein. Scale bar, 100 nm.
- I, J Some otoferlin-labelled structures bear clathrin coats (red arrowheads), suggesting that they originate from bulk endocytosis. Scale bar, 100 nm.
- K Otoferlin-labelled vesicles were on average larger in *Otof*^{I515T/I515T} IHCs (mean ± SEM; *Otof*^{I515T/I515T}, *n* = 86 vesicles, 18 images; *Otof*^{+/+}, *n* = 82 vesicles, 6 images; Wilcoxon rank-sum test; ****P* < 0.001).
- L Quantification of immunogold clusters at the plasma membrane revealed a strong trend towards reduced levels of otoferlin in *Otof*^{I515T/I515T} (six images each) (mean ± SEM; Wilcoxon rank-sum test).
- M Distal from the plasma membrane, immunogold labels were reduced in *Otof*^{I515T/I515T} IHCs (mean ± SEM; Kruskal–Wallis test; **P* < 0.05; ***P* < 0.01).
- N Representative electron micrographs of IHC ribbon synapses in *Otof*^{I515T/I515T} and *Otof*^{+/+} (conventional embedding without immunogold) after pre-incubation for 10 min at the indicated temperature followed by high K⁺ stimulation or 0 Ca²⁺ inhibition for 1 min 45 s. Scale bars, 100 nm.
- O Illustration depicting criteria for random section analysis (not drawn to scale). Ribbon-associated synaptic vesicles (SVs, green) in the first row ≤ 80 nm from ribbon (R) and membrane-proximal vesicles (yellow) in ≤ 25 nm membrane-to-membrane distance from the plasma membrane (blue) and ≤ 80 nm from each side of the presynaptic density.
- P, Q Synaptic vesicles with > 45 nm diameter appeared at 39°C in random sections; fraction of large membrane-proximal (P; Kruskal–Wallis test followed by non-parametric multiple comparison test; **P* < 0.05) and ribbon-associated (Q; one-way ANOVA followed by Tukey's test; **P* < 0.05; ***P* < 0.01) synaptic vesicles (mean ± SEM; *Otof*^{+/+} inhibitory, *n* = 24 synaptic ribbons, *Otof*^{+/+} stimulatory, *n* = 27 synaptic ribbons, *Otof*^{I515T/I515T} inhibitory, *n* = 36 synaptic ribbons, *Otof*^{I515T/I515T} stimulatory, *n* = 21 synaptic ribbons; see also Appendix Table S1).

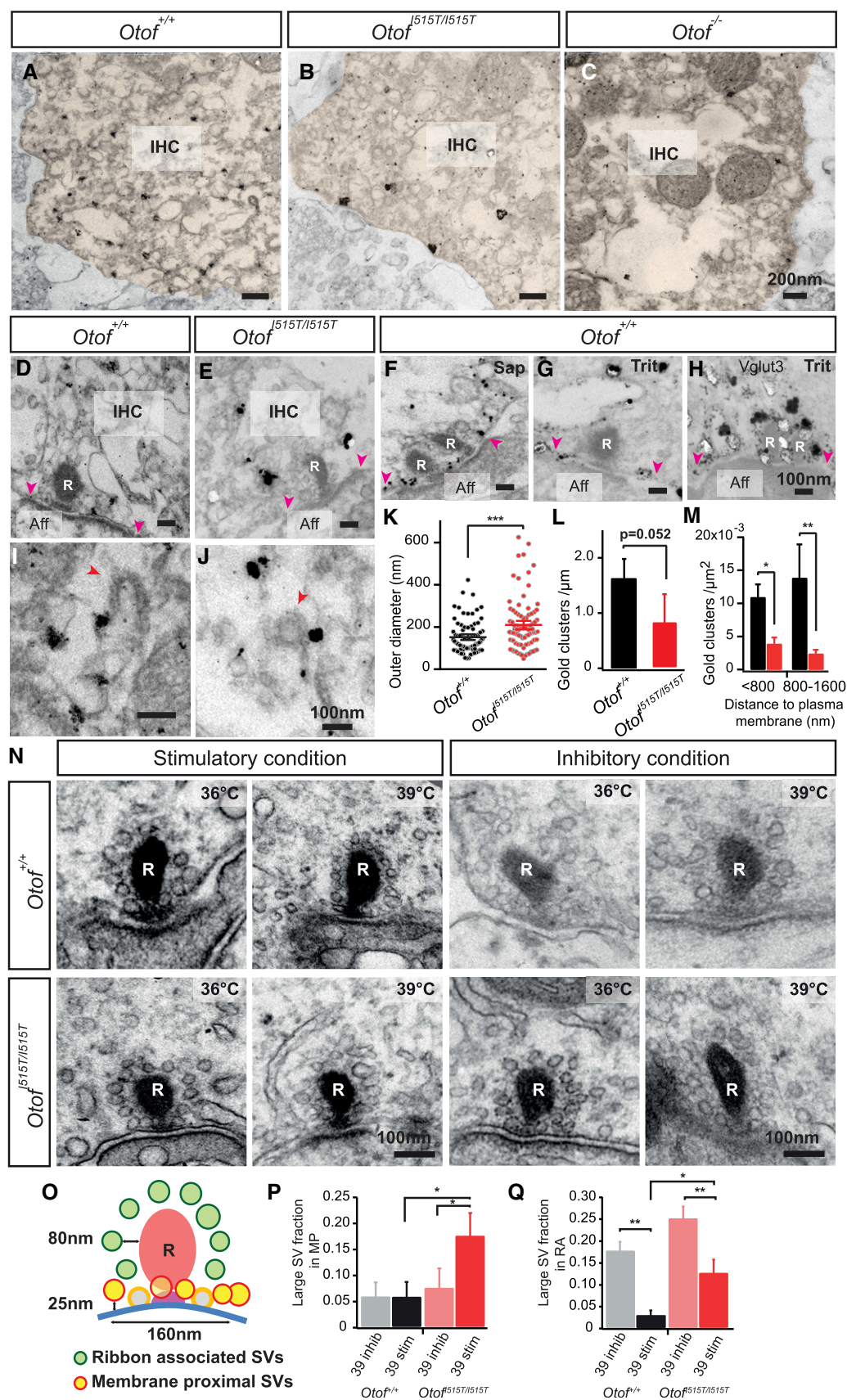


Figure 7.

genotypes ($N = 2$ mice/condition and genotype; Fig 7N and O, and Appendix Fig S6 and Appendix Table S1). The only significant effect was an increase in the number of membrane-proximal vesicles in *Otof*^{I515T/I515T} as compared to *Otof*^{+/+} IHCs after stimulation at either temperature (Appendix Table S1).

We next determined the vesicle diameter in all four conditions for both ribbon-associated and membrane-proximal vesicles. We found the majority of vesicle diameters to be in a 35–45 nm range, consistent with previous reports from IHC ribbon synapses (Neef et al, 2007; Appendix Fig S6). Remarkably, in the membrane-proximal pool at *Otof*^{I515T/I515T} synapses after stimulation at 39°C, vesicles with diameter > 45 nm were observed, that were less frequent after inhibition, and rarely observed in *Otof*^{+/+} (Fig 7P, Appendix Fig S6A and Appendix Table S1). In contrast, for the ribbon-associated pool, we found more large vesicles for inhibitory than for stimulatory condition at *Otof*^{+/+} (39°C) and, remarkably, even more for both conditions at *Otof*^{I515T/I515T} synapses (Fig 7Q, Appendix Fig S6B and Appendix Table S1).

We further analysed number and size of synaptic vesicles by performing electron tomography after stimulation at 36 and 39°C (Fig 8, $n = 4$ tomograms/genotype and condition; Table EV1). While the number of synaptic vesicles was unaltered in tomograms, we found the vesicles to be larger in *Otof*^{I515T/I515T} IHCs, both the membrane-proximal (Fig 8N and O) and the ribbon-associated ones (Fig 8P and Q). In all conditions tested, we also found some flattened vesicles (Table EV1), but their longest axis was not significantly different (Fig 8O and Q).

Together, the enlarged otoferlin-labelled endosomal vesicles and the enlarged synaptic vesicles point towards a deficit in vesicle reformation in *Otof*^{I515T/I515T} IHCs, which is more pronounced at febrile temperature.

Discussion

Here, we present a mouse model for auditory fatigue and otoferlin-related hearing impairment, allowing us to study the disease mechanism from molecular to systems level. Our analysis reveals that the remarkable IHC capability of indefatigable sustained exocytosis requires otoferlin. This likely involves roles of otoferlin in reformation of synaptic vesicles from endocytosed membrane as demonstrated here, in addition to tethering synaptic vesicles to the plasma membrane (Vogl et al, 2015), and priming and/or active zone clearance (Pangrsic et al, 2010; Jung et al, 2015). Presynaptic function of IHCs and sound encoding correlate with the abundance of otoferlin at the plasma membrane. We postulate that upon an elevation of the body temperature in human patients with temperature-sensitive *OTOF* mutations, properly folded otoferlin at the plasma membrane drops below a level critical for promoting synaptic sound encoding.

Hearing impairment correlates with the amount of otoferlin at the IHC plasma membrane

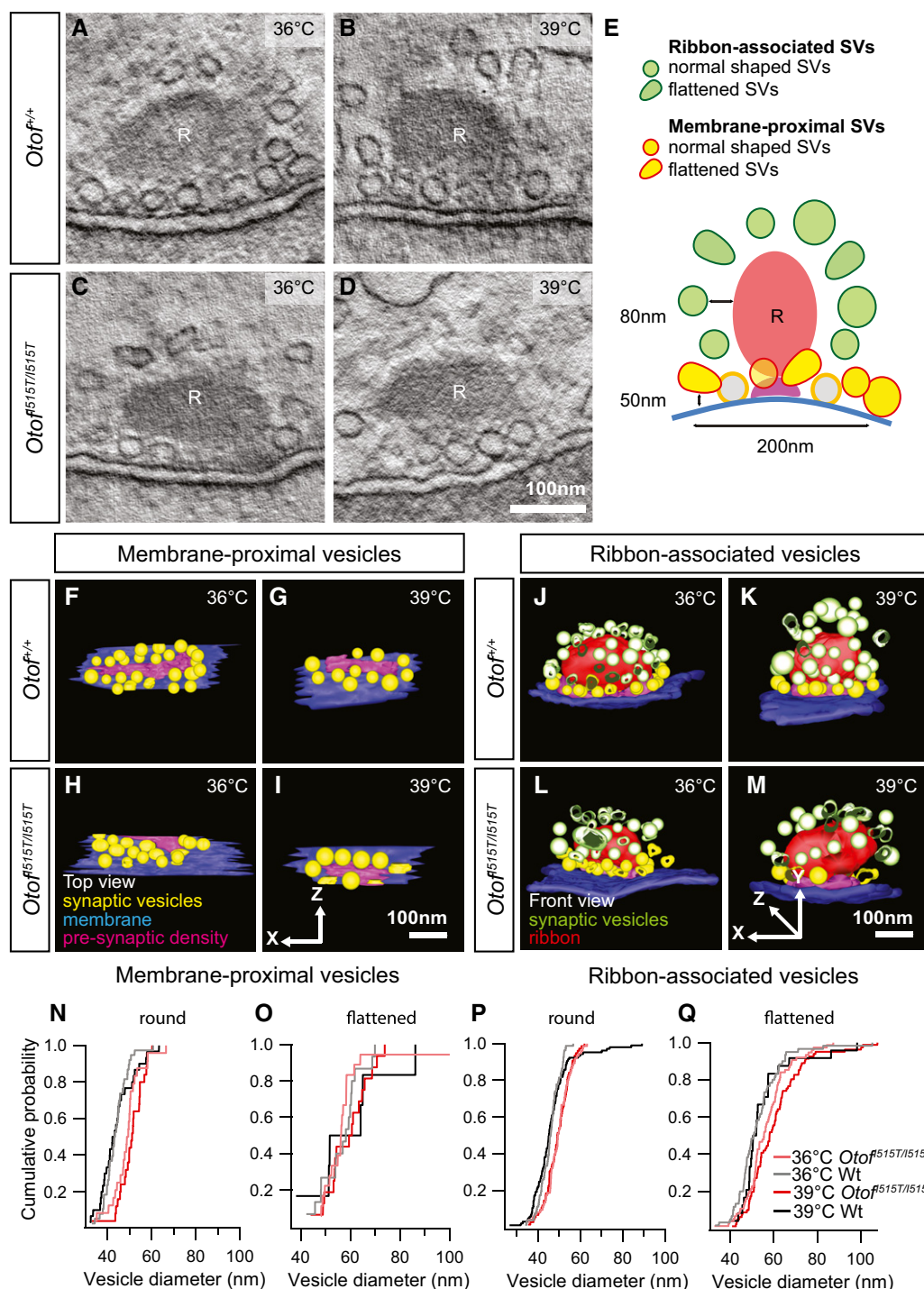
Most human *OTOF* mutations lead to profound deafness, but some patients have residual hearing. While two mouse missense mutants, *Otof*^{I515T/I515T} and *Otof*^{Pga/Pga}, show a similar overall reduction of otoferlin protein levels, *Otof*^{Pga/Pga} IHCs, in addition,

display a perturbed plasma membrane localization of otoferlin. This results in a reduction of absolute otoferlin membrane levels to only 3% of wild-type in *Otof*^{Pga/Pga} (Pangrsic et al, 2010 and this study), while *Otof*^{I515T/I515T} IHCs retain 34%. The comparison of the hearing phenotypes of *Otof*^{I515T/I515T}, *Otof*^{I515T/-}, *Otof*^{Pga/Pga} and *Otof*^{-/-} mice indicates that synaptic function and sound encoding scale with the amount of plasma membrane-bound otoferlin, which might generalize to human missense mutations. A further heat-induced reduction of the plasma membrane abundance of mouse Ile515Thr-otoferlin appeared rather slowly and the temperature-dependent hearing loss was relatively mild in *Otof*^{I515T/I515T} mice.

Direct comparison of mouse ABRs at febrile temperature with psychoacoustic testing of human patients is challenging. However, it seems that our mice are less susceptible to heat than human *OTOF*^{I515T/R1116*} subjects who exhibit a threshold elevation by ≥ 60 dB and loss of speech perception at 38.1°C body temperature. Our data indicate that this may be due to the RXR motif sequence presumably present in human otoferlin which reduces the plasma membrane abundance of Ile515Thr-otoferlin beyond what we found in *Otof*^{I515T/I515T} mice. The expression of this RXR motif depends on whether the first or the second splice acceptor site in exon 30 is used, which is currently unknown. Together, the lower cellular otoferlin protein levels due to the Ile515Thr mutation, the presumed presence of the RXR splice isoform, which causes a weaker potency of the Ile515Thr-otoferlin for plasma membrane localization, and a likely heat-induced protein unfolding provide a candidate mechanism for temperature-sensitive hearing loss in humans.

High rates of synaptic vesicle exocytosis at physiological temperature challenge current models for release mechanisms at ribbon synapses

Reconciling IHC physiological and morphological data with *in vivo* responses has remained difficult because of the clearly distinct experimental conditions (Buran et al, 2010; Pangrsic et al, 2010). Here, we set out to remove one important variable by combining data sets obtained near PT. Similar to a previous report (Nouvian, 2007), membrane capacitance estimates showed a ~threefold increase of exocytosis at PT compared to RT. Considering the *in vitro* patch clamp experiments at PT and assuming all exocytosis to occur at active zones, the calculated rate of sustained exocytosis amounts to ~2,300 vesicles/s/presynaptic active zone. This number appears very high when compared to EM counts of membrane- and ribbon-associated vesicles (on the order of 50/ribbon and with no obvious temperature dependence; Fig 8, Table EV1) and the average sustained SGN firing rate of 240 Hz in wild-type mice (Fig 4). Possible explanations for this discrepancy include more extrasynaptic exocytosis than described (Fuchs et al, 2003), a higher failure rate than assumed from *in vitro* and modelling studies (Siegel & Dallos, 1986; Rutherford et al, 2012) and/or synchronized multivesicular release. The mechanism of release at the hair cell synapse is a topic of active research and both synchronized multivesicular release (e.g. Glowatzki & Fuchs, 2002; Graydon et al, 2011) and univesicular release through a dynamic fusion pore (Chapochnikov et al, 2014) have been put forward to explain the heterogeneous size and shape of EPSCs. Based on modelling Graydon et al (2011) proposed synchronization of readily releasable vesicles by a common Ca^{2+}



nanodomain at frog hair cell active zones, which, however, seemed insufficient to explain large and fast EPSCs in a model of the rat IHC active zone (Chapochnikov *et al*, 2014). The comparable vesicle diameters in EM at RT and PT for *Otof*^{+/+} mice seemingly argue against homotypic fusion of synaptic vesicles, although a rapid exocytosis of such enlarged vesicles might have prevented their detection so far.

Otoferlin plays a key role for vesicle reformation

Using immunogold labelling, we found otoferlin at the plasma membrane (also reported in Roux *et al*, 2006) and, specifically, at the membrane of the active zones, which is consistent with a recent immunofluorescence analysis (Vogl *et al*, 2015). We found otoferlin labelling also at endosomal structures partially exhibiting budding of clathrin-coated vesicles, which is in agreement with STED fluorescence imaging data (Revelo *et al*, 2014), but not on synaptic vesicles of < 50 nm diameter. Remarkably, in *Otof*^{I515T/I515T} IHCs, we found enlarged otoferlin-labelled vesicular structures, potentially of endosomal origin, and on average larger synaptic vesicles after incubation both at 36 and 39°C. In contrast, deficiency of the otoferlin interacting molecule AP-2 μ , adapter protein for clathrin-mediated endocytosis, caused ablation of ribbon-associated vesicles distal from the active zone membrane, and a reduction of clathrin-coated structures close to ribbon synapses (Jung *et al*, 2015), indicating that otoferlin and AP-2 μ act on different steps of the vesicle reformation process.

In summary, we propose a new role for otoferlin in reformation of proper sized synaptic vesicles. The extent of the hearing loss in *Otof*^{I515T/I515T} might be explained by such a synaptic vesicle reformation defect, given that the high vesicle turnover rates at the IHC ribbon synapse require an ultrafast vesicle reformation mechanism. However, the impaired sustained exocytosis in *Otof*^{I515T/I515T} at RT points towards an additional deficit in priming (Pangrsic *et al*, 2010) and/or active zone clearance (Duncker *et al*, 2013; Jung *et al*, 2015).

Studying auditory fatigue at the level of single synapses in *Otof*^{I515T/I515T} mice

The normal size of the RRP observed in *Otof*^{I515T/I515T} IHCs *in vitro* seems in contrast to the SGN spike rate reduction *in vivo*. This discrepancy can be reconciled when considering that in the voltage clamp experiment, hyperpolarization allows for RRP recovery in the absence of Ca²⁺ influx-driven exocytosis, while *in vivo* spontaneous release diminishes the occupancy of the release sites that compose the RRP, reducing the “standing” RRP. Moreover, the lower time resolution of the capacitance recordings obscures the finding of a combined reduction of rate and synchronicity of sound onset firing which is observed in single unit recordings and highlighted by the ABR amplitude reduction.

At physiological temperature, the phenotype of *Otof*^{I515T/I515T} mice reproduces the clinical picture very well and single SGN response recordings in *Otof*^{I515T/I515T} mice provide an explanation for the apparent discrepancy between the normal sound sensitivity and the poor speech perception and ABRs in human patients: while few spikes from individual SGNs with normal thresholds may suffice for tone detection, the combination of reduced spike rates and higher jitter of action potential firing at sound onset can cause a

dramatic reduction in ABR wave I amplitude, as also observed in other mutants with impaired synaptic sound encoding (Buran *et al*, 2010). In response to constant or repetitive stimuli, *Otof*^{I515T/I515T} SGNs display markedly enhanced adaptation and slowed recovery from adaptation. This is consistent with the finding that patients with otoferlin deficiency show auditory fatigue when challenged with continuous sounds (Wynne *et al*, 2013). In contrast, none of the patient reports mention tinnitus as an additional symptom. We thus consider it unlikely that impairment of the perception of silent gaps in noise in our mice is due to tinnitus (Turner *et al*, 2006). Instead, it is likely explained by the combination of the reduction of adapted spike rates and the delayed recovery of the sound onset response. The resulting deficit in the encoding of fast fluctuations in sound envelope structure seems well consistent with the speech comprehension difficulties experienced by human patients which obviously cannot be restored by sound amplification using traditional hearing aids. Our data suggests that a more promising approach would be to devise a new speech processing strategy that aims to compensate for the increased adaptation. Clinicians should expect ABR latencies to be close to normal (Fig EV1B) and late ABR waves to be better preserved than wave I, suggesting partial compensation in the auditory brainstem. Finally, we suggest that tests for sound adaptation and temporal coding (e.g. gap detection) should be more generally applied in clinical settings to detect deficits that are independent of sound sensitivity.

Materials and Methods

Mouse genetics

Otof^{I515T/I515T} mice were generated by targeted mutagenesis of a genomic vector and homologous recombination in mouse embryonic stem cells (see Appendix Supplementary Methods for details).

Immunohistochemistry and quantification of fluorescence

Immunostaining and confocal fluorescence microscopy was performed essentially as described (Khimich *et al*, 2005) and detailed in Appendix Supplementary Methods.

For quantification of otoferlin and Vglut3 immunofluorescence, same experimental settings were used for each series. Using a *Matlab* routine implemented in *Imaris*, the cells were aligned in the xy- and yz-plane and the outer border of each cell was labelled manually in a 3D projection. Summed fluorescence intensities in voxels above or below the mid-nuclear plane were used for calculating the ratio of apical/basal fluorescence. Quantification of relative otoferlin membrane staining was performed after normalization of total cellular fluorescence levels and is illustrated in Fig 1D–F and was normalized to *Otof*^{+/+} values (at 37°C if applicable).

Pre-embedding immunogold labelling

Anti-otoferlin (Abcam, 1:300) and anti-Vglut3 (Synaptic Systems, 1:300) antibodies were applied after fixation and permeabilization with either saponin (Fig 7A–F, I and J) or Triton X-100 (Fig 7G and H). Silver enhancement was used prior to sample embedding, as described in Appendix Supplementary Methods.

Patch clamp recordings

IHCs from the apical coils of freshly dissected organs of Corti were patch-clamped in the perforated-patch configuration as described (Moser & Beutner, 2000). Experiments at elevated temperature and flash photolysis were performed as described (Beutner *et al*, 2001; Nouvian, 2007; respectively). For details, see Appendix Supplementary Methods.

Systems physiology and behaviour

ABRs, DPOAE and recordings from individual SGNs were performed as described (Jing *et al*, 2013), except for offline action potential detection which was based on spike waveform and amplitude using a custom-written *Matlab* routine (see Appendix Supplementary Methods for details). For ABR recordings with local temperature changes, ABRs in response to click stimuli at 60, 80 and 100 dB were measured using a custom-written *Matlab* routine controlling TDT system III (Tucker Davis Technologies) and a JBL 2402 speaker. A custom-designed heat probe (Appendix Fig S2A) was placed on the bony wall of the mouse bulla. The local temperature of the heat probe was constantly monitored, same for two miniaturized thermo-probes (H*MT, Newport Omega, Deckenpfronn) placed on the promontory wall within the bulla and in the mouth or in the cerebellum (accessed through a small hole in the occipital bone). Operant conditioning in the “Audiobox” was carried out essentially as described (de Hoz & Nelken, 2014), and startle responses were recorded and quantified as detailed in Appendix Supplementary Methods.

Electron microscopy and electron tomography

Organs of Corti (P14) were explanted in HEPES-Hanks solution and incubated for 1 min 45 s in pre-warmed Ca^{2+} free saline (5 mM K^+ , 0 Ca^{2+} and 5 mM EGTA; inhibitory condition) or in a solution containing 40 mM K^+ and 1.3 mM Ca^{2+} (stimulatory condition). Samples were fixed and prepared as described (Wong *et al*, 2014) and detailed in Appendix Supplementary Methods. For random section analysis, electron micrographs were acquired with transmission electron microscope (JEM-1011, 80 kV). For the 3D analysis, the semi-thin sections (250 nm) were imaged with JEM-2100 transmission electron microscope at 200 kV. Tomograms were reconstructed and analysed using *IMOD* package (bio3d.colorado.edu/imod/) and *ImageJ*. For details, see Appendix Supplementary Methods.

Molecular biology

Quantitative PCR, subcloning of full-length otoferlin cDNA from mouse organs of Corti and mutagenesis thereafter are described in Appendix Supplementary Methods, as transfection of IHCs or HEK cells and mass spectrometric quantification of otoferlin protein levels.

Statistics

The data were analysed using *Matlab* (Mathworks), *Microsoft Access* and *Excel*, the *Igor Pro 6* software package (WaveMetrics), *Origin 6.0*

(Microcal Software) and *GraphPad Prism*. Averaged data are expressed as mean \pm SEM unless otherwise specified. Normality was assessed using Jarque–Bera test for sample size of $n \geq 7$ and by Kolmogorov–Smirnov test for $n < 7$. For normally distributed samples, significance was tested using the unpaired, two-tailed Student's *t*-test, others with Mann–Whitney *U*-test, unless stated otherwise. Statistical significance of fluorescence immunohistochemistry and EM analysis was calculated by one-way ANOVA followed by Tukey–Newman–Keuls test for parametric and Kruskal–Wallis test followed by non-parametric multiple comparisons (NPMC).

Study approval

Animal handling and experiments complied with national animal care guidelines and were approved by the University of Goettingen Board for animal welfare and the animal welfare office of the state of Lower Saxony.

Expanded View for this article is available online.

Acknowledgements

We are especially grateful to Tobias Moser for generous support throughout the study. We thank Stefan Thom, Nina-Katrin Dankenbrink-Werder, Sandra Gerke and Christiane Senger-Freitag for expert technical assistance, Kirsten Reuter-Jessen for *pachanga* cDNA mutagenesis and help with stem cells, and Piotr Neumann, University of Goettingen, for providing model data and images of Appendix Fig S3. This work was supported by a Tandem Grant of the Max Planck Society (to N.B. and Tobias Moser), the Deutsche Forschungsgemeinschaft (DFG) through the Collaborative Research Center 889, projects A2 (Tobias Moser), A4 (E.R. and H.U.), A6 (N.S.), A7 (C.W.) and B1 (N.B.), as well as by DFG grant 2234/1-2 to RG-F and by the priority programme 1608 (N.S.). The University Medical Center Goettingen supported this work via a Heidenreich-von-Siebold fellowship to E.R. We thank Ulrich Müller and Martin Schwander for providing *pachanga* mouse mutants.

Author contributions

ER, NS and CW designed research; GH developed hard- and software; NS, RC, HA-M, ER, AM, TP, KTP and CL analysed data; NS, ER, RC, HA-M, AM, GY, CL, EA, TP and CW performed experiments; ER, NS, CW, RC, CL, AM, HA-M, TP and NB wrote and edited the manuscript; NS, ER, HA-M and RC prepared figures; ER, CW, NS, HU, NB and RG-F supervised research; ER and NS managed and coordinated the study; and NS, ER, CW, HU, RG-F and NB acquired funding.

Conflict of interest

The authors declare that they have no conflict of interest.

References

- Beutner D, Voets T, Neher E, Moser T (2001) Calcium dependence of exocytosis and endocytosis at the cochlear inner hair cell afferent synapse. *Neuron* 29: 681–690
- Buran BN, Strenzke N, Neef A, Gundelfinger ED, Moser T, Liberman MC (2010) Onset coding is degraded in auditory nerve fibers from mutant mice lacking synaptic ribbons. *J Neurosci Off J Soc Neurosci* 30: 7587–7597
- Chapochnikov NM, Takago H, Huang C-H, Pangršič T, Khimich D, Neef J, Auge E, Göttfert F, Hell SW, Wichmann C, Wolf F, Moser T (2014) Uniquantal

- release through a dynamic fusion pore is a candidate mechanism of hair cell exocytosis. *Neuron* 17: 1389–1403
- Chiu Y-H, Wu C-C, Lu Y-C, Chen P-J, Lee W-Y, Liu AY-Z, Hsu C-J (2010) Mutations in the OTOF gene in Taiwanese patients with auditory neuropathy. *Audiol Neurotol* 15: 364–374
- Duncker SV, Franz C, Kuhn S, Schulte U, Campanelli D, Brandt N, Hirt B, Fakler B, Blin N, Ruth P, Engel J, Marcotti W, Zimmermann U, Knipper M (2013) Otoferlin couples to clathrin-mediated endocytosis in mature cochlear inner hair cells. *J Neurosci* 33: 9508–9519
- Filipeanu CM, de Vries R, Danser AHJ, Kapusta DR (2011) Modulation of $\alpha 2C$ adrenergic receptor temperature-sensitive trafficking by HSP90. *Biochim Biophys Acta* 1813: 346–357
- Filipeanu CM, Pullikuth AK, Guidry JJ (2015) Molecular determinants of the human $\alpha 2C$ -adrenergic receptor temperature-sensitive intracellular traffic. *Mol Pharmacol* 87: 792–802
- Fuchs PA, Glowatzki E, Moser T (2003) The afferent synapse of cochlear hair cells. *Curr Opin Neurobiol* 13: 452–458
- Glowatzki E, Fuchs PA (2002) Transmitter release at the hair cell ribbon synapse. *Nat Neurosci* 5: 147–154
- Graydon CW, Cho S, Li G-L, Kachar B, von Gersdorff H (2011) Sharp Ca^{2+} nanodomains beneath the ribbon promote highly synchronous multivesicular release at hair cell synapses. *J Neurosci* 31: 16637–16650
- de Hoz L, Nelken I (2014) Frequency tuning in the behaving mouse: different bandwidths for discrimination and generalization. *PLoS ONE* 9: e91676
- Jing Z, Rutherford MA, Takago H, Frank T, Fejtova A, Khimich D, Moser T, Strenzke N (2013) Disruption of the presynaptic cytomatrix protein bassoon degrades ribbon anchorage, multiquantal release, and sound encoding at the hair cell afferent synapse. *J Neurosci* 33: 4456–4467
- Johnson CP, Chapman ER (2010) Otoferlin is a calcium sensor that directly regulates SNARE-mediated membrane fusion. *J Cell Biol* 191: 187–197
- Jung S, Maritzen T, Wichmann C, Jing Z, Neef A, Revelo NH, Al-Moyed H, Meese S, Wojcik SM, Panou I, Bulut H, Schu P, Ficner R, Reisinger E, Rizzoli SO, Neef J, Strenzke N, Haucke V, Moser T (2015) Disruption of adaptor protein 2 μ (AP-2 μ) in cochlear hair cells impairs vesicle reloading of synaptic release sites and hearing. *EMBO J* 34: 2686–2702
- Khimich D, Nouvian R, Pujol R, tom Dieck S, Egner A, Gundelfinger ED, Moser T (2005) Hair cell synaptic ribbons are essential for synchronous auditory signalling. *Nature* 434: 889–894
- Longo-Guess C, Gagnon LH, Bergstrom DE, Johnson KR (2007) A missense mutation in the conserved C2B domain of otoferlin causes deafness in a new mouse model of DFNB9. *Hear Res* 234: 21–28
- Marlin S, Feldmann D, Nguyen Y, Rouillon I, Loundon N, Jonard L, Bonnet C, Couderc R, Garabedian EN, Petit C, Denoyelle F (2010) Temperature-sensitive auditory neuropathy associated with an otoferlin mutation: deafening fever!. *Biochem Biophys Res Commun* 394: 737–742
- Matsunaga T, Mutai H, Kunishima S, Namba K, Morimoto N, Shinjo Y, Arimoto Y, Kataoka Y, Shintani T, Morita N, Sugiuchi T, Masuda S, Nakano A, Taiji H, Kaga K (2012) A prevalent founder mutation and genotype–phenotype correlations of OTOF in Japanese patients with auditory neuropathy. *Clin Genet* 82: 425–432
- Moser T, Beutner D (2000) Kinetics of exocytosis and endocytosis at the cochlear inner hair cell afferent synapse of the mouse. *Proc Natl Acad Sci USA* 97: 883–888
- Neef A, Khimich D, Piriš P, Riedel D, Wolf F, Moser T (2007) Probing the mechanism of exocytosis at the hair cell ribbon synapse. *J Neurosci* 27: 12933–12944
- Nouvian R (2007) Temperature enhances exocytosis efficiency at the mouse inner hair cell ribbon synapse. *J Physiol* 584: 535–542
- Pangrsic T, Lasarow L, Reuter K, Takago H, Schwander M, Riedel D, Frank T, Tarantino LM, Bailey JS, Strenzke N, Brose N, Müller U, Reisinger E, Moser T (2010) Hearing requires otoferlin-dependent efficient replenishment of synaptic vesicles in hair cells. *Nat Neurosci* 13: 869–876
- Pangrsic T, Reisinger E, Moser T (2012) Otoferlin: a multi-C2 domain protein essential for hearing. *Trends Neurosci* 35: 671–680
- Radziwon KE, June KM, Stolzberg DJ, Xu-Friedman MA, Salvi RJ, Dent ML (2009) Behaviorally measured audiograms and gap detection thresholds in CBA/CaJ mice. *J Comp Physiol A Neuroethol Sens Neural Behav Physiol* 195: 961–969
- Reisinger E, Bresee C, Neef J, Nair R, Reuter K, Bulankina A, Nouvian R, Koch M, Bückers J, Kastrup L, Roux I, Petit C, Hell SW, Brose N, Rhee J-S, Kügler S, Brigande JV, Moser T (2011) Probing the functional equivalence of otoferlin and synaptotagmin 1 in exocytosis. *J Neurosci Off J Soc Neurosci* 31: 4886–4895
- Revelo NH, Kamin D, Truckenbrodt S, Wong AB, Reuter-Jessen K, Reisinger E, Moser T, Rizzoli SO (2014) A new probe for super-resolution imaging of membranes elucidates trafficking pathways. *J Cell Biol* 205: 591–606
- Romanos J, Kimura L, Fávero ML, Izarra FAR, de Mello Auricchio MTB, Batisso AC, Lezirovitz K, Abreu-Silva RS, Mingroni-Netto RC (2009) Novel OTOF mutations in Brazilian patients with auditory neuropathy. *J Hum Genet* 54: 382–385
- Roux I, Safieddine S, Nouvian R, Grati M, Simmler M-C, Bahloul A, Perfettini I, Le Gall M, Rostaing P, Hamard G, Triller A, Avan P, Moser T, Petit C (2006) Otoferlin, defective in a human deafness form, is essential for exocytosis at the auditory ribbon synapse. *Cell* 127: 277–289
- Rutherford MA, Chapochnikov NM, Moser T (2012) Spike encoding of neurotransmitter release timing by spiral ganglion neurons of the cochlea. *J Neurosci* 32: 4773–4789
- Schwander M, Sczaniecka A, Grillet N, Bailey JS, Avenarius M, Najmabadi H, Steffy BM, Federe GC, Lagler EA, Banan R, Hice R, Grabowski-Boase L, Keithley EM, Ryan AF, Housley GD, Wiltshire T, Smith RJH, Tarantino LM, Müller U (2007) A forward genetics screen in mice identifies recessive deafness traits and reveals that pejkakin is essential for outer hair cell function. *J Neurosci* 27: 2163–2175
- Siegel JH, Dallos P (1986) Spike activity recorded from the organ of Corti. *Hear Res* 22: 245–248
- Starr A, Sininger Y, Winter M, Derebery MJ, Oba S, Michalewski HJ (1998) Transient deafness due to temperature-sensitive auditory neuropathy. *Ear Hear* 19: 169–179
- Turner JG, Brozoski TJ, Bauer CA, Parrish JL, Myers K, Hughes LF, Caspary DM (2006) Gap detection deficits in rats with tinnitus: a potential novel screening tool. *Behav Neurosci* 120: 188–195
- Varga R, Kelley PM, Keats BJ, Starr A, Leal SM, Cohn E, Kimberling WJ (2003) Non-syndromic recessive auditory neuropathy is the result of mutations in the otoferlin (OTOF) gene. *J Med Genet* 40: 45–50
- Varga R, Avenarius MR, Kelley PM, Keats BJ, Berlin CI, Hood LJ, Morlet TG, Brashears SM, Starr A, Cohn ES, Smith RJH, Kimberling WJ (2006) OTOF mutations revealed by genetic analysis of hearing loss families including a potential temperature sensitive auditory neuropathy allele. *J Med Genet* 43: 576–581
- Vogl C, Cooper BH, Neef J, Wojcik SM, Reim K, Reisinger E, Brose N, Rhee J-S, Moser T, Wichmann C (2015) Unconventional molecular regulation of synaptic vesicle replenishment in cochlear inner hair cells. *J Cell Sci* 128: 638–644
- Wang D-Y, Wang Y-C, Weil D, Zhao Y-L, Rao S-Q, Zong L, Ji Y-B, Liu Q, Li J-Q, Yang H-M, Shen Y, Benedict-Alderfer C, Zheng Q-Y, Petit C, Wang Q-J (2010) Screening mutations of OTOF gene in Chinese patients with auditory neuropathy, including a familial case of temperature-sensitive auditory neuropathy. *BMC Med Genet* 11: 79

- Wong AB, Rutherford MA, Gabrielaitis M, Pangršič T, Göttfert F, Frank T, Michanski S, Hell S, Wolf F, Wichmann C, Moser T (2014) Developmental refinement of hair cell synapses tightens the coupling of Ca^{2+} influx to exocytosis. *EMBO J* 33: 247–264
- Wynne DP, Zeng F-G, Bhatt S, Michalewski HJ, Dimitrijevic A, Starr A (2013) Loudness adaptation accompanying ribbon synapse and auditory nerve disorders. *Brain J Neurol* 136: 1626–1638
- Yasunaga S, Grati M, Cohen-Salmon M, El-Amraoui A, Mustapha M, Salem N, El-Zir E, Loiselet J, Petit C (1999) A mutation in OTOF, encoding otoferlin, a FER-1-like protein, causes DFNB9, a nonsyndromic form of deafness. *Nat Genet* 21: 363–369
- Yildirim-Baylan M, Bademci G, Duman D, Ozturkmen-Akay H, Tokgoz-Yilmaz S, Tekin M (2014) Evidence for genotype-phenotype correlation for OTOF mutations. *Int J Pediatr Otorhinolaryngol* 78: 950–953